Helical versus collinear antiferromagnetic order tuned by magnetic anisotropy in polar and chiral $(Ni,Mn)_3TeO_6$

Jaewook Kim,[1,2,*] J. Yang,[3] C. J. Won,[4] Kyoo Kim,[2] Bongjae Kim,[5] D. Obeysekera,[3] Dong Woo Lee,[2] and Sang-Wook Cheong[1,4]

[1]*Rutgers Center for Emergent Materials and Department of Physics and Astronomy, Rutgers University, Piscataway, New Jersey 08854, USA*

[2]*Korea Atomic Energy Research Institute, Daejeon 34057, Republic of Korea*

[3]*Department of Physics, New Jersey Institute of Technology, Newark, New Jersey 07102, USA*

[4]*Laboratory for Pohang Emergent Materials and Max Plank POSTECH Center for Complex Phase Materials, Pohang University of Science and Technology, Pohang 37673, Republic of Korea*

[5]*Department of Physics, Kunsan University, Gunsan 54150, Republic of Korea*

(Received 7 June 2021; accepted 31 August 2021; published 13 September 2021)

Polar and chiral Ni_3TeO_6 was found to exhibit a colossal magnetoelectric (ME) effect associated with collinear antiferromagnetic order. We have investigated the evolution of its magnetic state with the substitution of the Ni^{2+} spins by isotropic Mn^{2+} spins, namely $(Ni, Mn)_3TeO_6$ (NMTO). The ground state of NMTO maintains an Ising nature, but a new phase with XY-type magnetic anisotropy is discovered at an intermediate temperature range. Neutron powder diffraction experiments reveal that (1) Mn ions tend to occupy a specific transition-metal site, consistent with the first-principle calculation, and (2) the intermediate phase is an incommensurate (IC) helical magnetic state propagating along the c axis with $\vec{q}_{IC} = (0,\ 0,\ 1.5 \pm \delta)$. We also found that the balance between these two magnetic states can be readily manipulated with magnetic fields, which results in significant ME effects. This selective site occupancy of NMTO allows for a unique competition between collinear and helical magnetic structures with minimal chemical disorder. Thus, NMTO serves as a model system to study site-specific chemical control of noncollinear magnetism and ME coupling.

DOI: 10.1103/PhysRevMaterials.5.094405

I. INTRODUCTION

Noncentrosymmetric crystal structure (polar or chiral) allows for antisymmetric magnetic exchange interaction, also known as Dzyaloshinskii-Moriya (DM) interaction $\overrightarrow{D_{12}} \cdot (\overrightarrow{S_1} \times \overrightarrow{S_2})$ ($\overrightarrow{D_{12}}$: Dzyaloshinskii vector between spins $\overrightarrow{S_1}$ and $\overrightarrow{S_2}$), which originates from the spin-orbit coupling and absence of inversion symmetry [1,2]. It allows for noncollinear spin arrangement and may stabilize chiral magnetic structures such as conical, helical, cycloidal, and skyrmion states [3–5], which are of intense study over the past decades [6]. These states give rise to various emergent properties such as magnetically induced ferroelectric polarization and strong magnetoelectric (ME) coupling [7–10], anomalous/topological Hall effect [11–14], and nonreciprocal effects [15,16]. Skyrmions, in particular, are stable topological quasiparticles in mesoscale and have great potential in future device applications [6].

In addition to the DM interaction, formation of these unconventional magnetic structures strongly depends on the constituent magnetic spins. For example, intercalated transition-metal dichalcogenide (TMDC) materials with chiral space group display plethora of magnetic ground states within $3d$ transition metal ions; helical [17,18], Ising ferromagnet [19,20], Ising antiferromagnet [21], and collinear antiferromagnet [22]. Thus, chemical composition plays an important role in determining the magnetic ground state as much as the crystal symmetry. In this regard, chemical mixing of dissimilar magnetic ions seem to be a promising route to introduce competition between different magnetic ground states and search for emergent phases and/or functionality. However, it is mostly accompanied by chemical disorder with short range magnetic interactions, making it difficult to study its intrinsic properties.

Orthotellurate Ni_3TeO_6 (NTO), which crystallizes in a noncentrosymmetric space group $R3$ [23,24], is both *polar and chiral* and may circumvent the issue of chemical disorder and provides a platform to study the effect of magnetic anisotropy under chemical doping. It orders to a commensurate collinear (CC) antiferromagnet (AFM) with an Ising-type magnetic anisotropy below 51 K [25]. Upon application of high magnetic field along the magnetic easy axis, it shows a "nonhysteretic" spin-flop type transition with strong ME coupling at ~9 T [26] and another transition at higher magnetic field with stronger ME effect [27]. Optical spectroscopy study showed that the 9 T transition in NTO involves changes in crystal-field environment of Ni^{2+} and accompanies sensitive magneto-optical response [28]. Neutron scattering study revealed that the spin-flop type transition is actually a first-order phase transition and the "spin-flopped" phase is, in fact, an incommensurate (IC) spin-helical state where spins lie in the ab plane and rotate along the c axis [29].

*jaewook@kaeri.re.kr

Recent reports show that it is possible to partially substitute Ni with other 3*d* transition metal ions (M = Mn, Co) and still preserve its noncentrosymmetric space group $R3$. By Mn doping, magnetic ordering temperature (T) increases as high as ∼70 K, but the system is reported to order magnetically the same as NTO [30,31]. On the other hand, upon Co doping, the system orders to an IC spin-helical ground state, similar to the magnetic field-induced spin-helical state of NTO [32]. Both systems exhibit low-energy excitations below T_N with intricate spin-lattice coupling, possibly electromagnons [31,32].

Here, in contrast to previous Mn-doping studies [30,31], we discovered a new magnetic state under zero magnetic field by Mn doping in NTO, namely $Ni_{3-x}Mn_xTeO_6$ (NMTO). We find the solubility limit of Mn into the NTO matrix up to $x < 1.0$, above which a phase separation occurs with Mn_3TeO_6 phase (space group $R\bar{3}$). Compared to the previous work [31], both our single- and polycrystalline samples below $x = 1.0$ are free from impurities. The new magnetic phase is actually an IC spin-helical phase that emerges between AFM ordering temperature (T_N) ∼ 75 and ∼65 K under zero magnetic field, below which a CC AFM phase persists to lowest temperature measured, identical to the case of NTO. Interestingly we find a sharp peak at the IC spin helical to CC AFM transition and a broad feature under magnetic field-induced transition in dielectric susceptibility (ε) measurements, indicating strong ME coupling. Neutron powder diffraction (NPD) experiment reveals that the Mn ions mostly occupy a specific site among three possible crystallographic positions for M ions. We performed a density-functional theory calculation and compared the formation energies of a model NMTO system with Mn ions occupying different transition-metal sites. Our work demonstrates a viable route to realize the modulated spin structures in noncentrosymmetric magnets, between Ising- and XY-type magnetic anisotropies, which can be useful for future applications.

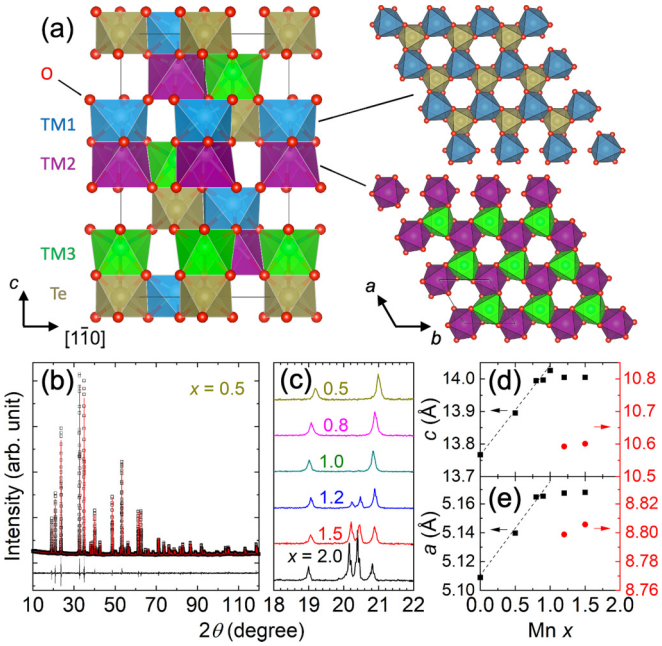

FIG. 1. (a) Crystal structures of $Ni_{3-x}Mn_xTeO_6$ (NMTO) viewed along (left) the [110] direction and (right) the [001] direction, showing TM1-Te and TM2-TM3 layers in the *ab* plane. Three transition metals (TM)-oxygen (red spheres) cages are shown in blue, purple, and green, respectively. Te-oxygen cages are shown in dark yellow. (b) XRD data taken at room temperature and Rietveld refinement on a powder sample with $x = 0.5$. Black symbols, red, and green lines represent observed intensity, fitted intensity, and the difference between the observed and fitted intensity, respectively. (c) XRD data of powder samples with different Mn dopings (x). (d) and (e) Lattice parameters from Rietveld refinement of XRD and NPD data at room temperature as a function of x. Black and red symbols are from phases with space groups $R3$ and $R\bar{3}$, respectively. Dashed linear lines are guides to the eye.

II. METHODS

NMTO powder samples were prepared by solid state reaction method [25]. Stoichiometric amounts of NiO (99.9% purity), $MnCO_3$ (99.99%), and TeO_2 (99.99%) were ground and sintered at 800 °C for 24 h, followed by furnace cooling to room temperature. The process was repeated twice with an intermediate grinding. Single crystals of NMTO were grown by chemical vapor transport (CVT) technique with polycrystalline powder and $TeCl_4$ as transport agent. We found that the growth of single crystals with desired phase (space group $R3$) is rather insensitive to Ni/Mn ratio of the polycrystalline powder used for CVT, although larger Mn concentration in the polycrystal yields Mn_3TeO_6 impurities (space group $R\bar{3}$) which is discussed later. Powder x-ray diffraction (XRD) was measured using a Cu $K\alpha$ source at room temperature (X'Pert Pro, PANalytical). Single-crystal XRD data were collected at $T = 173$ K using graphite-monochromated Mo $K\alpha$ radiation (PHOTON II X-ray diffractometer, Bruker). Single crystals obtained have planar hexagonal shape with typical edge length and thickness of 0.7 and 0.1 mm, respectively [Fig. 1(b)]. Prior to the bulk measurement, samples were examined under a polarized optical microscope to ensure that they have a single polar/chiral domain.

We used a commercial cryostat equipped with a superconducting magnet (Physical Property Measurement System, Quantum Design) for dielectric, electric polarization, and specific heat measurements. Electrodes for dielectric and electric polarization experiments were made by Au sputtering. Dielectric constant was measured by using an LCR meter (7600, Quadtech) at frequencies between 440 Hz and 440 kHz. Electric polarization was measured using an electrometer (617, Keithely). Magnetic susceptibility was measured using either a superconducting quantum interferometer (Magnetic Properties Measurement System, Quantum design) or a vibrating sample magnetometer (Quantum Design). The crystal and magnetic structure of NMTO powder sample with the mass of ∼10 g were investigated using neutron diffraction method at high-resolution powder diffractometer (BT-1) at the NIST Center for Neutron Research. NPD experiments were performed in a T range from 300 to 4 K with a wavelength of 2.079 Å (Ge-311 monochromator). NPD data were analyzed using Rietveld refinement program FullProf suite. The Simulated Annealing and Representation Analysis (SARAh) program was used to derive the symmetry allowed magnetic structures [33,34].

III. RESULTS

A. Structural characterization by x-ray diffraction

NMTO with $x < 1$ adopts the same space group ($R3$) as NTO [23–25]. Ni and Mn ions occupy three distinct crystallographic sites, denoted as TM1, TM2, and TM3. As shown in Fig. 1(a), all three TM sites and Te ions are surrounded with six oxygen ions forming distorted octahedrons. Each TM1-TM2 and TM3-Te ion pairs are linked by face-sharing oxygen planes along the c axis, forming columns of TM1-TM2-□-TM3-Te (□ denotes the empty oxygen octahedra along the c axis). In the ab plane, TM1-Te and TM2-TM3 ions are connected through two oxygen ions and form a planar honeycomb lattices of edge-sharing octahedra. Each pairing ions are slightly shifted along the c axis with respect to the center of the octahedra. These two adjacent layers are repeated along the c axis with a relative in-plane shift by (1/3, 1/3, 0) in the unit cell.

Figure 1(b) shows the XRD data of a powder NMTO sample with $x = 0.5$ and its Rietveld refinement result ($\chi^2 = 2.09$), adopting the structural model of NTO (details of the refinement is included in the Supplemental Material [35]). However, upon further increasing the Mn concentration x from 1.0, we find additional peaks as shown in Fig. 1(c). For $x = 0.5$, 0.6, and 1.0, two peaks are observed at ~19° and 21° that corresponds to (003) and (101) reflections within the space group $R3$, respectively. On top of these peaks, two extra peaks with weak intensity are observed in $x = 1.0$ sample at 20.2° and 20.4°, which increases in intensity concomitantly up to $x = 2.0$. We identify these extra peaks with others in different angles (not shown) as second phases as reported for Mn_3TeO_6 with space group $R\bar{3}$ [36]. Thus, the solubility limit of Mn in NTO is slightly below $x = 1.0$ (at least grown by solid state reaction method), above which the sample shows phase separation. Figures 1(d) and 1(e) show the evolution of lattice constants c and a as a function of x, respectively. Up to $x = 1$, both a and c lattice constants increase linearly in x, following Vegard's law, with a single phase. The linear relation does not hold above $x = 1.2$ and both a and c values of the $R3$ phase remain more-or-less constant up to $x = 1.5$.

B. Bulk physical properties

Having identified the single-phase limit of NMTO, we studied its bulk physical properties. Figure 2 shows the T-dependent magnetic susceptibility (χ) of powder sample with $x = 0.9$ under different applied magnetic fields. A large hump observed at 75 K marks the onset of a long-range AFM order (T_{N1}) which is the largest value among pure and doped M_3TeO_6 series [30–32]. Upon cooling below T_{N1}, a small kink feature is observed at $T_{N2} = 63$ K at $\mu_0 H = 1$ T, indicating another magnetic phase transition in NMTO. This kink behavior becomes larger and broader in T with increasing applied magnetic field and disappears at 6 T.

In order to understand the nature of the new magnetic phase, we studied a single crystal sample grown by CVT method in detail. Exact Mn concentration x of the single-crystal sample can be estimated by comparing its c axis lattice constant (13.93 Å), obtained by calculation of single crystal XRD data (see the Supplemental Material for details [35]), with the trend in polycrystal samples [Fig. 1(d)] where we find $x \sim 0.60$. Bulk physical properties of this sample are summarized in Fig. 3. From χ and specific heat (C_p) curves [Figs. 3(a) and 3(b)], we find that a long-range magnetic order sets in at $T_{N1} = 74$ K. At $T > T_{N1}$, $\chi(T)$ curves with magnetic field applied along the ab plane and c axis directions overlap nicely, following the Curie-Weiss behavior with $T_{CW} = -8.9$ K and $\mu_{eff} = 3.4\ \mu_B/M$.

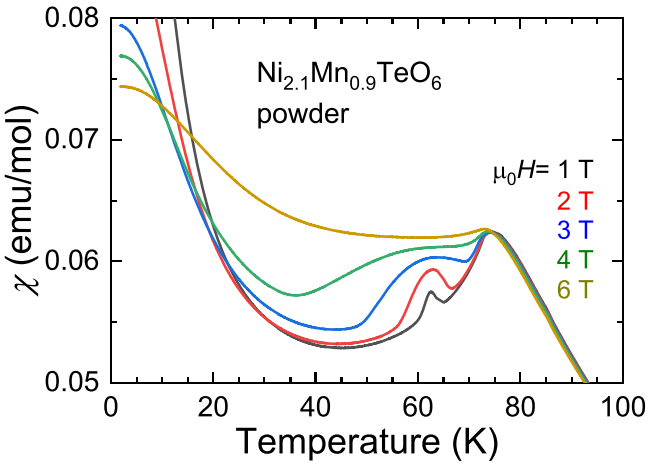

FIG. 2. Magnetic susceptibility of $Ni_{2.9}Mn_{0.1}TeO_6$ powder sample as a function of temperature under different magnetic fields.

Below T_{N1}, two curves show anisotropic T dependencies as shown in Fig. 3(a). For $H \parallel ab$, upon cooling, χ shows a hump at T_{N1} and an upward step at $T_{N2} = 60$ K. For $H \parallel c$, χ is constant between T_{N1} and T_{N2} with a step down at T_{N2} on cooling. These features indicate that, between T_{N2} and T_{N1}, magnetic moments are aligned along the ab plane with XY-type magnetic anisotropy. Below T_{N2}, they are aligned along the c axis with Ising-type anisotropy, similar to what is observed in NTO [25]. The specific heat curve [Fig. 3(b)] shows two features that correspond to these transitions: a large λ-like peak at T_{N1} and a small one at T_{N2}. The small peak at T_{N2} implies that the phase transition at T_{N2} involves a minute entropy change.

Both magnetic transitions are also observed in dielectric properties as shown in the T dependencies of change of electric polarization (ΔP) [Fig. 3(c)] and dielectric constant (ε) [Figs. 3(d) and 3(e)] measured along the c axis. Below T_{N1}, electric polarization emerges and increases upon cooling down to lowest T at $H = 0$. $\Delta P(T)$ curve shows a small kink at T_{N2} which is also observable at $\mu_0 H = 4.5$ and 5 T, but none at 9 T. Electric polarization developed below T_{N1} is not reversible by switching the poling electric field direction above T_{N1}, indicating that this system is not ferroelectric as reported in NTO [26]. The maximum ΔP value reaches 565 $\mu C/m^2$ at 2 K and $H = 0$.

To further track the evolution of the new magnetic state in magnetic field, we studied the T dependence of ε in detail. In zero magnetic field, T_{N1} and T_{N2} show a small hump and a large peak, respectively. When magnetic field is applied along the ab plane direction [Fig. 3(d)], the peak at T_{N2} diminishes in size and merges with T_{N1} above 3 T. Multiple features are observed when magnetic field is applied along the c axis. With

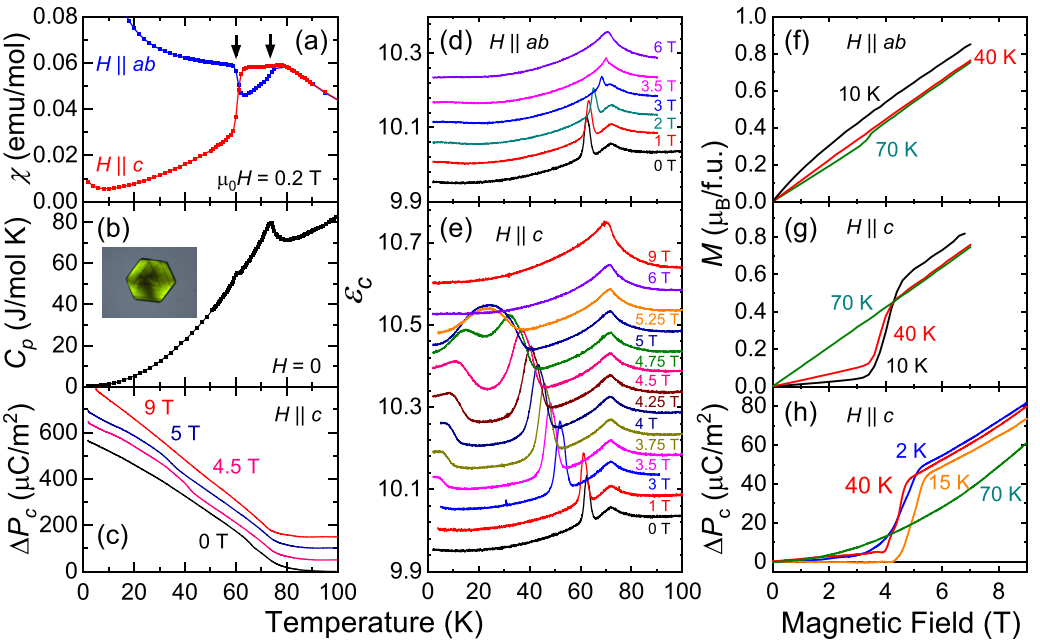

FIG. 3. Bulk physical properties of the NMTO single crystal with $x = 0.60$. Temperature-dependent (a) magnetic susceptibilities along two different crystallographic directions, (b) specific heat, (c) change of electric polarization [$\Delta P \equiv P(T) - P(T = 100\ \mathrm{K})$] along the c axis, and (d) and (e) dielectric constants along the c axis with magnetic field applied along two different crystallographic directions. Magnetic field dependence of (f) and (g) magnetization as a function of magnetic field along the ab plane and c axis, (h) change of electric polarization [$\Delta P \equiv P(H) - P(H = 0)$] along the c axis at different temperatures. Arrows in (a) mark T_{N1} and T_{N2} as described in text. Data in (c), (d), and (e) are shifted for clarity. Photo in (b) shows a single crystal with edge length of $\sim$400 μm.

increasing magnetic field, the peak in T_{N2} increases in size and shifts to lower T. Above 3.5 T, ε increases on further cooling to lowest temperature and manifests a shoulderlike feature. As magnetic field increases, this shoulder feature expands to higher T and merges with the peak at T_{N2} as a wide broad bump at 5.25 T, with its maximum at $T = 24$ K. Finally, the merged bump quickly disappears as magnetic field increases further. In both magnetic field directions, T_{N1} value is independent of magnetic field value up to 9 T.

Magnetic field-dependent magnetization curves show the field-induced magnetic transitions. At 10 K, the magnetization along the ab plane increases monotonically up to 7 T, similar to the case of NTO with easy-axis anisotropy [26,27]. However, at 70 K, when the system is in the easy-plane anisotropy phase, magnetization shows a small kink at 3.5 T and increases linearly up to 7 T [Fig. 3(f)]. For c axis magnetic field, it shows a rather broad transition centered at $\sim$4 T at 10 and 40 K. But at 70 K, when the system is in the easy-plane anisotropy phase, it increases linearly in H. We note that at 10 K, the $M(H)$ curve along the ab direction shows a Brillouin-type PM background. Similarly, $M(H)$ curve at 10 K along the c axis above 4 T shows a linear behavior which does not extrapolate to $M = 0$ at 0 T. These observations indicate that there may exist orphan spins in the system, which are subject to local exchange interactions. This feature is also observable in $\chi(T)$ curve along the ab direction [Fig. 3(a)].

Change of electric polarization (ΔP) measured along the c direction with magnetic field applied along the same direction shows a strong ME coupling in this material. ΔP jumps in a similar manner as the c axis magnetization. Interestingly, the change is sharper in magnetic field at 15 K, rather than at lower temperatures, e.g., 2 K. We do not find any clear signature of hysteresis in magnetic field for both magnetization and electric polarization across the phase transition.

The three different phases in H-T phase diagram observed in NMTO under different magnetic field orientations are summarized in Fig. 4. Phase boundaries are determined by marking the anomaly positions in T dependencies of χ, ε, and C_p curves, and the peak in $\frac{dM}{dH}(H)$, respectively. We note that the $\frac{dM}{dH}(H)$ curves show a broad peak feature; e.g., at 10 K, the transition ranges from 3–5 T with the peak centered at 4 T (not shown). We denote the phases above T_N and the ground state as paramagnet (PM) and CC AFM, respectively. The intermediate phase is identified as IC spin helical which will be discussed in the next section. By increasing the in-plane H [Fig. 4(a)], the temperature window of the IC helical phase quickly diminishes and is no longer observed above $\sim$5 T. On the other hand, the IC helical phase is stabilized with increasing out-of-plane magnetic field [Fig. 4(b)]. At $T < 20$ K, a broad hump in the dielectric constant shows up, implying a reentrant phase transition. We note that this behavior is concomitant with the broad magnetic transition observed in $M(H)$ data [Fig. 3(g)].

C. Neutron powder diffraction

To understand this new magnetic phase, we performed neutron powder diffraction (NPD) measurements at different temperatures. Figure 5(a) shows the NPD pattern obtained from a powder sample with $x = 0.9$ at $T = 300$ K. Rietveld refinement was performed and all of the diffraction peaks could be indexed using the space group $R3$, as in NTO

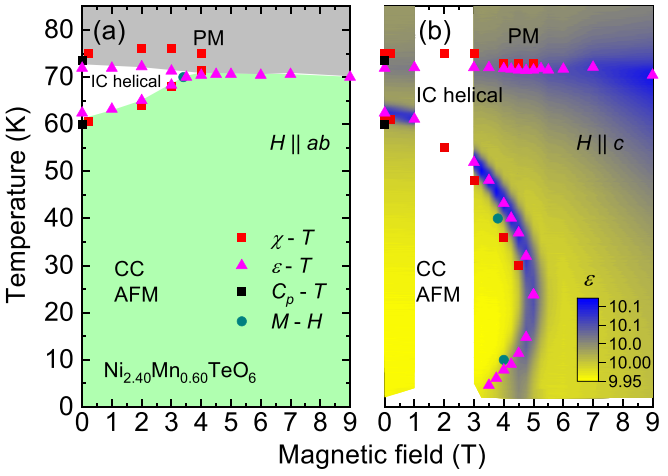

FIG. 4. H-T phase diagram of NMTO single crystal ($x = 0.60$) with magnetic-field applied along the (a) ab plane and (b) c axis, based on data presented in Fig. 3. (b) Contour plot of ε taken from $\varepsilon(T)$ data [Fig. 3(e)] is also shown. Red, magenta, black, and dark cyan symbols indicate phase transition points determined from magnetic susceptibility, dielectric constant, specific heat, and magnetization measurements, respectively. PM, IC helical, and CC AFM denote paramagnetic, incommensurate spin helical, and commensurate collinear antiferromagnetic phases, respectively.

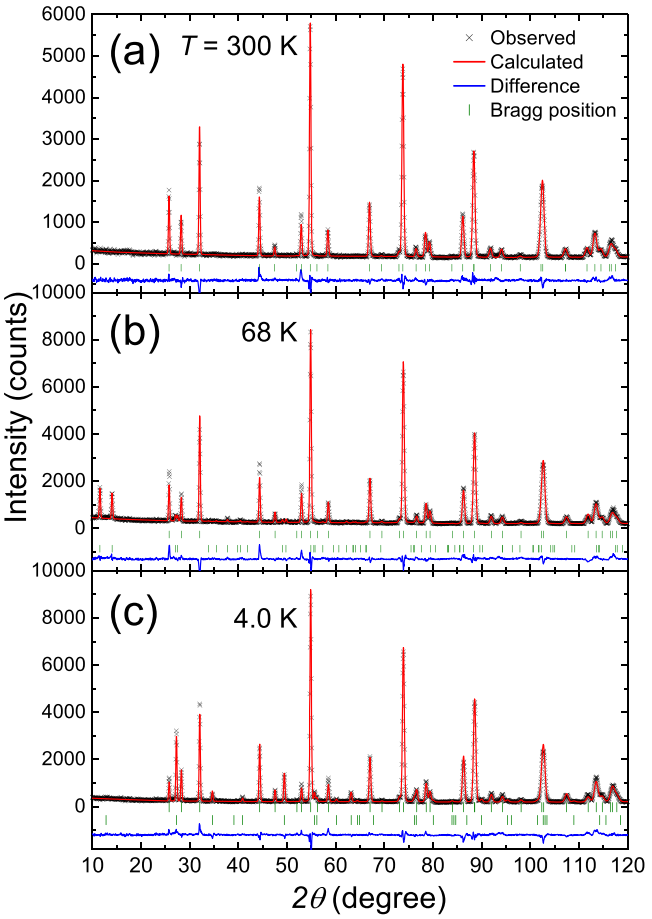

FIG. 5. Neutron powder diffraction data of NMTO ($x = 0.9$) sample at different temperatures. Position indicators in the upper and lower columns in (b) and (c) denote the Bragg positions for lattice and magnetic structures, respectively.

[25] with the unit cell parameters $a = 5.1656(4)$ Å and $c = 13.9970(4)$ Å. Overall occupancies of Ni and Mn ions for this specimen were determined to be 2.100(3) and 0.899(7), respectively. Best fit result ($\chi^2 \sim 2.9$) shows that TM1 site is fully occupied by Ni ions while Mn ions partially substitute Ni ions in TM2 and TM3 sites with more tendency in the TM2 site (see Table I). The models in which Mn ions mainly occupy TM1 site or TM3 site always result in a χ^2 larger than 10. For models in which Mn ions occupy both TM2 and TM3 sites, when increasing the occupancy of Mn ions at TM3 site from 0.25119 to 0.64851, the χ^2 increases from 2.9 to 13.0. The model with Mn ions with occupancies of 0.64851 at TM2 site and 0.25119 at TM1 site gives χ^2 of 6.8. These comparisons clearly confirms the preferred occupancy of Mn ions at TM2 site. Refinement result also indicate that the c position of TM2 ions shift towards TM1, while it shifts away from in the case of other isostructural systems [31,32,36]. However, we note that the goodness of the fit is insensitive to the c position, which might be due to the site mixing.

Magnetic reflections emerge upon cooling below T_{N1}. Figures 5(b) and 5(c) show the observed and calculated NPD patterns at 68 and 4 K, respectively. All the magnetic reflections can be indexed with the crystal structure in space group $R3$ symmetry with proper magnetic propagation vectors. In the $T_{N2} < T < T_{N1}$ range, incommensurate magnetic peaks appear at $2\theta = 11.554°$ and 14.061°. The propagation vector was determined as $k = (0, 0, 1.5 \pm \delta)$ with $\delta = 0.146$. The microscopic magnetic structures compatible with the crystal symmetry can be obtained from group-theory analysis. Using the program of SARAh, the basis vectors of the irreducible representations that leave the propagation vector invariant were calculated and listed in Table II. Γ1 describes the spin alignment along the c axis, while Γ2 and Γ3 give solutions to that along the ab plane. Since the $\chi(T)$ curves suggest

TABLE I. Structural parameters for NMTO ($x = 0.9$) sample, obtained from NPD data taken at 300 K.

Atom	Wycoff site	x	y	z	Occupation
Ni1	3a	0.00000	0.00000	0.68943	1.00000
Ni2/Mn2	3a	0.00000	0.00000	0.49008	0.35151/0.64850
Ni3/Mn3	3a	0.00000	0.00000	0.19923	0.74871/0.25119
Te	3a	0.00000	0.00000	0.00536	1.00000
O1	9b	0.30350	0.01167	0.08742	1.00000
O2	9b	0.66285	−0.04654	0.59567	1.00000

TABLE II. Basis vectors for the space group $R3{:}H$ with $k = (0, 0, 1.354)$.

		BV components					
IR	BV	*ma*	*mb*	*mc*	*ima*	*imb*	*imc*
	ψ_1	0	0	0	0	0	0
Γ1	ψ_2	0	0	0	0	0	0
	ψ_3	0	0	3	0	0	0
	ψ_4	1.5	0	0	−0.866	−1.732	0
Γ2	ψ_5	0	1.5	0	1.732	0.866	0
	ψ_6	0	0	0	0	0	0
	ψ_7	1.5	0	0	0.866	1.732	0
Γ3	ψ_8	0	1.5	0	−1.732	−0.866	0
	ψ_9	0	0	0	0	0	0

an alignment of magnetic moments along the *ab* plane between T_{N2} and T_{N1}, we employ Γ2 symmetry to describe the magnetic structure in this region. All the nuclear and magnetic reflections and intensities can be well fitted yielding $m_{\mathrm{Ni}} = 0.85(1)\ \mu_B$ and $m_{\mathrm{Mn}} = 2.10(8)\ \mu_B$ ($\chi^2 = 4.29$). The refinement using Γ3 yields a similar magnetic structure with similar magnetic moments and χ^2. The combination of Γ2 and Γ3 does not improve the refinement result. For simplicity we use the Γ2 symmetry to describe the magnetic structure of NMTO in the $T_{N2} < T < T_{N1}$ range. Here the spin structure is described by an IC helical model with spins aligned in the *ab* plane which are stacked along the *c* axis, as shown in Fig. 6(a).

Below T_{N2}, the IC magnetic reflections disappear and all reflections can be indexed with space group *R*3 unit cell with a CC AFM magnetic propagation vector $k = (0, 0, 1.5)$, identical to those reported earlier [25,29,32]. The $\chi(T)$ curves suggest an alignment of magnetic moments along the *c* axis below T_{N2} which is only compatible with Γ1 symmetry. Spin structure model is shown in Fig. 6(b). The intensities of all the nuclear and magnetic reflections at 4 K can be best fitted employing the Γ1 magnetic structure with the fit yielding $m_{\mathrm{Ni}} = 1.794\ \mu_B$ and $m_{\mathrm{Mn}} = 3.355\ \mu_B$ ($\chi^2 = 3.12$).

D. Density functional calculation

In order to understand the preferential site occupancy of Mn in TM sites in NMTO, we performed density functional theory (DFT) calculations on pure Ni_3TeO_6 and Ni_2MnTeO_6 with different Mn substitution configurations, where Mn substitutes Ni in one of three TM sites. We adopted Dudarev's DFT+U scheme implemented in VASP package. The effective Coulomb potentials (U) of 5.0 and 6.5 eV for Mn and Ni atoms have been used, respectively, with Perdew-Burke-Ernzerhof exchange correlation potentials. K-point mesh 5×5×2 with energy cut of 450 eV is used for all the calculations. We assumed full occupation of TM sites and collinear AFM magnetic ground state as observed in NPD experiment.

The lowest energy configuration is found when Mn ions occupy TM2 site. The energy differences (ΔE), i.e., relative formation energy, to the ground state (Mn in TM2) configuration are ΔE(Mn in TM1) = +0.4 eV/f.u. and ΔE(Mn in TM3) = +0.2 eV/f.u. This result is consistent with NPD result in overall (Table I): Mn occupation fraction is largest in TM2 site (∼65%), smaller in TM1 site (∼25%), and none in TM1 site.

By comparing the partial density-of-states (pDOS) of Ni_3TeO_6 and Ni_2MnTeO_6 (Fig. 7), we can clearly observe the doping effect of Mn. The most noticeable effect is that Mn *d* orbitals form an emergent in-gap state, which is located in between the *d*-*d* gap of Ni, hence reducing the gap size and dominating the low-energy physics. The occupied *d* orbitals of TM are well hybridized with *p* orbitals of oxygen.

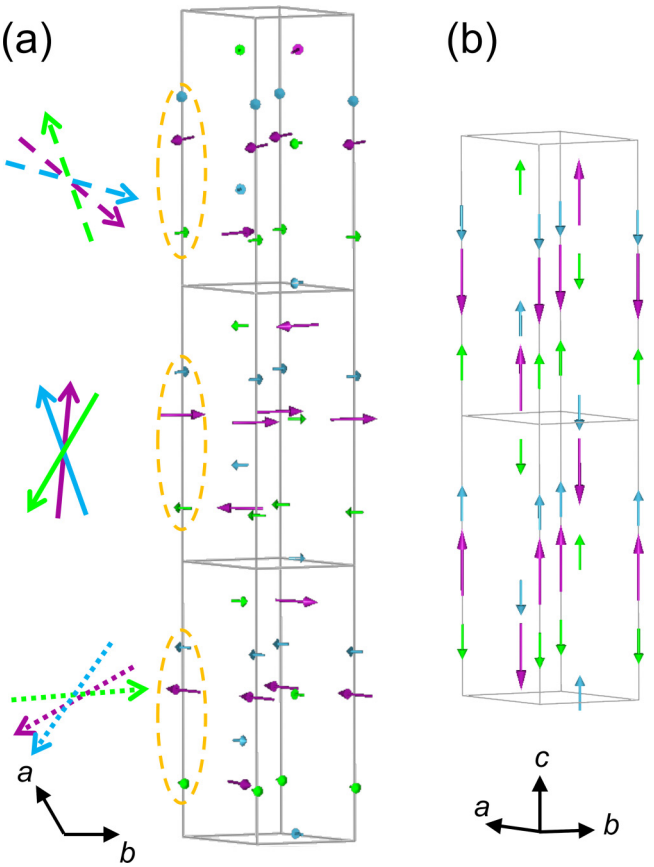

FIG. 6. Schematic spin structures deduced from neutron powder diffraction data at (a) 68 K and (b) 4 K, respectively. Left column in (a) shows top view of spin directions inside orange dashed circles in each unit cell. Blue, purple, and green arrows denote the spins on TM1, TM2, and TM3 sites, respectively.

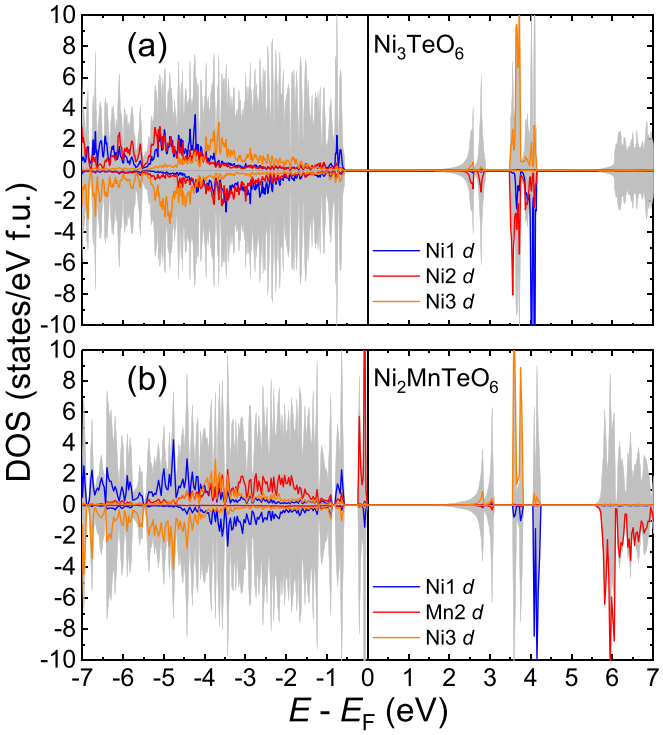

FIG. 7. Total and partial density-of-states of (a) Ni_3TeO_6, and (b) Ni_2MnTeO_6 with Mn occupying the TM2 site. Gray shaded region indicate the total DOS while blue, red, and orange solid lines indicate pDOS of d orbitals in three different TM sites.

IV. DISCUSSION

Observation of two magnetic states implies a strong competition between CC AFM and IC helical state in NMTO. Previous study on the same system only found the CC AFM ordered phase, possibly due to the phase separation of Ni_3TeO_6 and Mn_3TeO_6 [31], as we observed in our samples with $x > 1$ [Figs. 1(c)–1(e)]. Another study on Co-doped NTO, reported an IC helical spin structure [32], but it orders into a single spin-helical state down without any other magnetic phases. Doping studies on other $3d$ magnetic transition metal ions into NTO have not been reported to date, perhaps due to strong tendency to form M_2TeO_6 phase with M = Cr, Fe [37]. Thus, NMTO serves as a unique example that manifests two ordered magnetic states by chemical mixing.

It is interesting that three IC helical states in NTO and its derivatives with space group $R3$, display similar IC magnetic wave vector $(0, 0, q_{IC})$: pure NTO with applied magnetic field along c axis above ∼9 T ($q_{IC} = 1.32$) [29], Co-doped NTO ($q_{IC} = 1.211$–1.299, depending on Co doping level) [32], and Mn-doped NTO ($q_{IC} = 1.354$, this work). For the former two cases, a simplified magnetic Hamiltonians qualitatively explain the experimentally observed field-induced transition, helical wave vector, magnon spectrum, and electric polarization under magnetic field [27,29]. On the other hand, thermally stabilized spin-helical state in NMTO, as we report here, suggests that not only exchange interaction and magnetic anisotropy but also thermal fluctuation plays a crucial role in its formation. Such a description is applied to weakly anisotropic magnetic materials with cubic or tetrahedral crystal systems to explain modulated spin structure, including magnetic skyrmions [4,5]. We speculate that introducing DM interaction or free energy analysis is necessary to explain this phenomenon.

Although, both IC helical phases of NTO and NMTO exhibit similar bulk physical properties, there are some notable differences. First, the "spin-flop" transition in NMTO is broad in magnetic field and occurs at ∼4 T at 10 K, compared to a sharp jump that occurs at 9 T, 2 K in NTO [26]. Furthermore, the phase diagram of NMTO shows a reentrant behavior at $T < 25$ K [Fig. 4(b)] as determined from the $\varepsilon(T)$ curves. For $H \parallel c$, dielectric constant increase above 3 T upon cooling below 8 K. When magnetic field is further increased, the low temperature dielectric constant anomaly becomes a shoulder and gradually merges to the CM-ICM phase transition at 5.25 T. This trend in dielectric constant is markedly different from field-induced behavior in NTO, where dielectric constant increases monotonically on cooling and do not display any kink or shoulder behavior up to the spin-flop magnetic field [26,28].

The broad feature in ε at low T, magnetic field-induced transition, and the reentrant behavior observed in H-T phase diagram suggests that structural/magnetic disorder between Ni and Mn may play a role. However, frequency-dependent dielectric (40 Hz to 400 kHz) measurements (not shown) did not show any frequency dependence, ruling out ferroelectric diffuse phase transition as the source of the broad feature.

Typically, intermixing of magnetic ions with different anisotropies leads to the suppression of magnetic order and/or onset of short-range interactions. For example, recent works on intermixing of $MnPS_3$ and $NiPS_3$ report that magnetic order is greatly suppressed to low temperature, close to half-mixing composition without any emergent magnetic phases [38,39]. Thus, enhanced AFM ordering temperature and a sharp phase transition between IC helical and collinear AFM phase in NMTO are rather unique phenomenon. We attribute this behavior to three distinct crystallographic sites in this double corundum system [23], which can be selectively substituted by different magnetic ions, although the energy differences between each configurations are small in energy, as we show in our DFT calculation. The origin of this site preference requires further investigation. Future sample synthesis with other magnetic ions may help understand this intricate behavior.

V. CONCLUSION

Our systematic synthesis of polycrystalline samples of NMTO shows that it remains in the space group $R3$ with polar/chiral point group up to a certain doping level ($x < 1$). In this doping regime, by combining bulk characterization of single crystals, we find a new spin state with easy-plane, XY-type magnetic anisotropy at zero magnetic field in an intermediate temperature range, which accompanies a strong ME effect at the temperature or magnetic field-induced phase transitions. Neutron powder diffraction reveals that this XY-type anisotropic phase is an IC spin-helical structure, similar to those observed in magnetic field-induced state in pure NTO and Co-doped NTO [29,32]. From DFT calculation we find that Mn ions occupy a specific crystallographic site (TM2) in NMTO, suggesting that this system can have mixed

composition with minimal disorder. In addition, a unique in-gap state of Mn *d* orbitals is predicted from band structure calculation. Other chemical substitutions would be of interest to induce other exotic magnetic states. Our work proves a chemical sensitivity of polar magnets to induce unconventional magnetic states. Site specific doping suggests new design principles in polar magnets.

ACKNOWLEDGMENTS

We thank H. S. Kim, V. Kiryukhin, X. Xu, and J. Y. Kim for helpful discussions. Works at Rutgers University and NJIT are supported by the U.S. Department of Energy, Office of Basic Energy Sciences under DE-FG02-07ER46382, and DE-SC0021188, respectively. This work was also supported by National Research Foundation of Korea with Awards No. 2021R1C1007017 (B.K.), No. 2016K1A4A4A01922028, No. 2020M3H4A2084417 (C.J.W.), and No. 2021M2E3A3040092 (D.W.L.). J.K. and K.K. acknowledge the support from KAERI Internal R&D program (524460-21). We thank C. Brown for help carrying out the neutron diffraction experiments. J.K. thanks S. S. Lee and S. H. Lim for assisting XRD analyses. We acknowledge the support of the National Institute of Standards and Technology, U.S. Department of Commerce, in providing the neutron research facilities used in this work.

[1] I. E. Dzyaloshinsky, A thermodynamic theory of weak ferromagnetism of antiferromagnetics, J. Phys. Chem. Solids **4**, 241 (1958).

[2] T. Moriya, Anisotropic superexchange interaction and weak ferromagnetism, Phys. Rev. **120**, 91 (1960).

[3] A. Bogdanov and A. Hubert, Thermodynamically stable magnetic vortex states in magnetic crystals, J. Magn. Magn. Mater. **138**, 255 (1994).

[4] A. N. Bogdanov, U. K. Rößler, M. Wolf, and K.-H. Müller, Magnetic structures and reorientation transitions in noncentrosymmetric uniaxial antiferromagnets, Phys. Rev. B **66**, 214410 (2002).

[5] A. N. Bogdanov and C. Panagopoulos, Physical foundations and basic properties of magnetic skyrmions, Nat. Rev. Phys. **2**, 492 (2020).

[6] N. Nagaosa and Y. Tokura, Topological properties and dynamics of magnetic skyrmions, Nat. Nanotechnol. **8**, 899 (2013).

[7] S. W. Cheong and M. Mostovoy, Multiferroics: A magnetic twist for ferroelectricity, Nat. Mater. **6**, 13 (2007).

[8] T. Kimura, Spiral magnets as magnetoelectrics, Annu. Rev. Mater. Res. **37**, 387 (2007).

[9] Y. Tokura and S. Seki, Multiferroics with spiral spin orders, Adv. Mater. **22**, 1554 (2010).

[10] T.-h. Arima, Spin-driven ferroelectricity and magneto-electric effects in frustrated magnetic systems, J. Phys. Soc. Jpn. **80**, 052001 (2011).

[11] I. Martin and C. D. Batista, Itinerant Electron-Driven Chiral Magnetic Ordering and Spontaneous Quantum Hall Effect in Triangular Lattice Models, Phys. Rev. Lett. **101**, 156402 (2008).

[12] S. D. Yi, S. Onoda, N. Nagaosa, and J. H. Han, Skyrmions and anomalous Hall effect in a Dzyaloshinskii-Moriya spiral magnet, Phys. Rev. B **80**, 054416 (2009).

[13] N. Nagaosa, J. Sinova, S. Onoda, A. H. MacDonald, and N. P. Ong, Anomalous Hall effect, Rev. Mod. Phys. **82**, 1539 (2010).

[14] S. Nakatsuji, N. Kiyohara, and T. Higo, Large anomalous Hall effect in a non-collinear antiferromagnet at room temperature, Nature (London) **527**, 212 (2015).

[15] S.-W. Cheong, D. Talbayev, V. Kiryukhin, and A. Saxena, Broken symmetries, non-reciprocity, and multiferroicity, npj Quantum Mater. **3**, 19 (2018).

[16] Y. Tokura and N. Nagaosa, Nonreciprocal responses from non-centrosymmetric quantum materials, Nat. Commun. **9**, 3740 (2018).

[17] T. Miyadai, K. Kikuchi, H. Kondo, S. Sakka, M. Arai, and Y. Ishikawa, Magnetic properties of $Cr_{1/3}NbS_2$, J. Phys. Soc. Jpn. **52**, 1394 (1983).

[18] Y. Kousaka, Y. Nakao, J. Kishine, M. Akita, K. Inoue, and J. Akimitsu, Chiral helimagnetism in $T_{1/3}NbS_2$ (T = Cr and Mn), Nucl. Instrum. Methods Phys. Res. Sect. A **600**, 250 (2009).

[19] M. Eibschütz, S. Mahajan, F. J. DiSalvo, G. W. Hull, and J. V. Waszczak, Ferromagnetism in metallic intercalated compounds Fe_xTaS_2 ($0.20 \leqslant x \leqslant 0.34$), J. Appl. Phys. **52**, 2098 (1981).

[20] S. Mangelsen, J. Hansen, P. Adler, W. Schnelle, W. Bensch, S. Mankovsky, S. Polesya, and H. Ebert, Large anomalous Hall effect and slow relaxation of the magnetization in $Fe_{1/3}TaS_2$, J. Phys. Chem. C **124**, 24984 (2020).

[21] O. Gorochov, A. L. Blanc-soreau, J. Rouxel, P. Imbert, and G. Jehanno, Transport properties, magnetic susceptibility and Mössbauer spectroscopy of $Fe_{0.25}NbS_2$ and $Fe_{0.33}NbS_2$, Philos. Mag. B **43**, 621 (2006).

[22] S. S. P. Parkin, E. A. Marseglia, and P. J. Brown, Magnetic structure of $Co_{1/3}NbS_2$ and $Co_{1/3}TaS_2$, J. Phys. C **16**, 2765 (1983).

[23] R. E. Newnham and E. P. Meagher, Crystal structure of Ni_3TeO_6, Mater. Res. Bull. **2**, 549 (1967).

[24] R. Becker and H. Berger, Reinvestigation of Ni_3TeO_6, Acta Cryst. E **62**, i222 (2006).

[25] I. Zivkovic, K. Prsa, O. Zaharko, and H. Berger, Ni_3TeO_6—A collinear antiferromagnet with ferromagnetic honeycomb planes, J. Phys.: Condens. Matter **22**, 056002 (2010).

[26] Y. S. Oh, S. Artyukhin, J. J. Yang, V. Zapf, J. W. Kim, D. Vanderbilt, and S. W. Cheong, Non-hysteretic colossal magnetoelectricity in a collinear antiferromagnet, Nat. Commun. **5**, 3201 (2014).

[27] J. W. Kim, S. Artyukhin, E. D. Mun, M. Jaime, N. Harrison, A. Hansen, J. J. Yang, Y. S. Oh, D. Vanderbilt, V. S. Zapf, and S. W. Cheong, Successive Magnetic-Field-Induced Transitions and Colossal Magnetoelectric Effect in Ni_3TeO_6, Phys. Rev. Lett. **115**, 137201 (2015).

[28] M. O. Yokosuk, A. al-Wahish, S. Artyukhin, K. R. O'Neal, D. Mazumdar, P. Chen, J. Yang, Y. S. Oh, S. A. McGill, K. Haule, S.-W. Cheong, D. Vanderbilt, and J. L. Musfeldt, Magnetoelectric Coupling through the Spin Flop Transition in Ni_3TeO_6, Phys. Rev. Lett. **117**, 147402 (2016).

[29] J. Lass, C. R. Andersen, H. K. Leerberg, S. Birkemose, S. Toth, U. Stuhr, M. Bartkowiak, C. Niedermayer, Z. Lu, R. Toft-Petersen, M. Retuerto, J. O. Birk, and K. Lefmann, Field-induced magnetic incommensurability in multiferroic Ni_3TeO_6, Phys. Rev. B **101**, 054415 (2020).

[30] R. Mathieu, S. A. Ivanov, P. Nordblad, and M. Weil, Enhancement of antiferromagnetic interaction and transition temperature in M_3TeO_6 systems (M = Mn, Co, Ni, Cu), Eur. Phys. J. B **86**, 361 (2013).

[31] M. Retuerto, S. Skiadopoulou, F. Borodavka, C. Kadlec, F. Kadlec, J. Prokleska, Z. Deng, J. A. Alonso, M. T. Fernandez-Diaz, F. O. Saouma, J. I. Jang, D. Legut, S. Kamba, and M. Greenblatt, Structural and spectroscopic properties of the polar antiferromagnet Ni_2MnTeO_6, Phys. Rev. B **97**, 144418 (2018).

[32] S. Skiadopoulou, M. Retuerto, F. Borodavka, C. Kadlec, F. Kadlec, M. Míek, J. Prokleka, Z. Deng, X. Tan, C. Frank, J. A. Alonso, M. T. Fernandez-Diaz, M. Croft, F. Orlandi, P. Manuel, E. McCabe, D. Legut, M. Greenblatt, and S. Kamba, Structural, magnetic, and spin dynamical properties of the polar antiferromagnets $Ni_{3-x}Co_xTeO_6$ ($x = 1, 2$), Phys. Rev. B **101**, 014429 (2020).

[33] A. S. Wills, A new protocol for the determination of magnetic structures using simulated annealing and representational analysis (SARAh), Phys. B: Condens. Matter **276–278**, 680 (2000).

[34] A. S. Wills, Indexing magnetic structures and crystallographic distortions from powder diffraction: Brillouin zone indexing, Z. Kristallogr. Suppl. **2009**, 39 (2009).

[35] See Supplemental Material at http://link.aps.org/supplemental/10.1103/PhysRevMaterials.5.094405 for refinement parameters for powder and single-crystal XRD data described in text.

[36] M. Weil, Mn_3TeO_6, Acta Cryst. E **62**, i244 (2006).

[37] W. Kunnmann, S. La Placa, L. M. Corliss, J. M. Hastings, and E. Banks, Magnetic structures of the ordered trirutiles Cr_2WO_6, Cr_2TeO_6 and Fe_2TeO_6, J. Phys. Chem. Solids **29**, 1359 (1968).

[38] R. Basnet, A. Wegner, K. Pandey, S. Storment, and J. Hu, Highly sensitive spin-flop transition in antiferromagnetic van der Waals material MPS_3 (M = Ni and Mn), Phys. Rev. Mater. **5**, 064413 (2021).

[39] Y. Shemerliuk, Y. Zhou, Z. Yang, G. Cao, A. U. B. Wolter, B. Buchner, and S. Aswartham, Tuning magnetic and transport properties in quasi-2D $(Mn_{1-x}Ni_x)_2P_2S_6$ single crystals, Electron. Mater. **2**, 284 (2021).